Stochastic models of dense or hollow nanoparticles and their scattering properties

Cedric J Gommes,[a]* Raphael Chattot[b] and Jakub Drnec[b]

[a]Department of Chemical Engineering, University of Liège B6A, 3 Allée du six Août, B-4000 Liège, Belgium, and [b]ID31, European Synchrotron Radiation Facility, 71 Avenue des Martyrs, 38000 Grenoble France. E-mail: Cedric.Gommes@uliege.be

Small-Angle Scattering, form factors, hollow nanoparticles, disordered structures, Gaussian random fields

Abstract

We propose a family of stochastic models of disordered particles, obtained by clipping a Gaussian random field with a function that is space-dependent. Depending on the shape of the clipping function, dense or hollow particles can be modelled. We derive general expressions for the form factor of the particles, for their average volume and surface area, as well as for their density and surface-area distributions against the distance to the particle centre. We also introduce a general approximation for the form factor based on the density and surface-area distributions, which coincides with the Guinier and Porod expressions in the limits of low and high scattering vector q. The models are illustrated with the fitting of Small-Angle X-ray Scattering (SAXS) data measured on Pt/Ni hollow nanoparticles. Our SAXS analysis and modelling notably capture the collapse of the particles porosity after being used as oxygen-reduction catalysts.

1. Introduction

Small-angle scattering (SAS) of x-rays (SAXS) or neutrons (SANS) is a very versatile experimental method that enables one to characterize the structure of nanomaterials over length scales that range from 1 nm to 100 nm, in a wide variety of chemical and physical environments (Glatter & Kratky, 1982; Stribeck, 2010). Moreover, this can often be done in a time-resolved way both for synchrotron SAXS (Narayanan *et al.*, 2001; Grillo, 2009) and for SANS (Pipich *et al.*, 2008; Carl *et al.*, 2020). However, a significant difficulty with small-angle scattering is the data analysis. There generally exists a variety of structures that are compatible with a given scattering pattern (Gommes *et al.*, 2012), so that converting scattering data into meaningful structural information requires models (Pedersen, 1997).

When developing models to analyse SAS data from disordered materials, one has always to find a trade-off between conceptual simplicity and realism. The former is needed for the robust analysis of scattering patterns with as few parameters as possible. The latter ensures that as many structural characteristics as possible are accounted for in the materials description. This is particularly challenging in the case of disordered materials, the structure of which is partially random. For this type of materials, stochastic models offer a practical way through the almost antagonistic requirements of geometrical realism and mathematical simplicity (Gommes, 2018).

In this paper we introduce a family of stochastic models of either dense or hollow particles, obtained by clipping a Gaussian random field with a function that is space-dependent. The well-known Gaussian random field model of biphasic materials (Quiblier, 1984; Berk, 1987; Teubner, 1991; Chen *et al.*, 1996; Levitz, 1998) is obtained as a particular case of the present general family of models for constant clipping functions. We derive general analytical expressions for volume and surface area of the particles, for their density and area profiles, as well as for their form factors.

The derivations are limited here to a material with uniform scattering contrast, but the modelling procedure can be generalised to multiple phases as well. We illustrate the practical use of these models for SAXS data analysis with the case of PtNi hollow nanoparticles supported of carbon, used as oxygen reduction catalysts.

2. Experimental

The theoretical developments of the present paper were motivated by the SAXS analysis of PtNi hollow nanoparticles supported on Vulcan XC72 porous carbon. Details for the preparation of PtNi nanoparticles and membrane electrode assembly (MEA) sample can be found in Chattot *et al.* (2018) and Chattot *et al.* (2020), respectively.

Proton-Exchange Membrane (PEM) fuel-cell accelerated stress test was conducted in a dedicated single 5 cm^2 cell, controlled by a test station (FCS-4M-100W, Lean-Cat Fuel Cell) and a Biologic SP-400 potentiostat. First, the cell was operated at 80 °C, under H_2/Air at 150 sccm/350 sccm flow rate (atmospheric pressure) for anode/cathode and the humidification rate was 100%. The MEA was quickly conditioned for about 1h by maintaining a cell voltage of 0.6 V. Then, the gas at cathode was switched to N_2, and 5000 square wave potential cycles between 0.6 V and 1.1 V (3s - 3s) were applied. Since the anode consisted in Pt nanoparticles in equilibrium under H_2, the cathode cell potential vs. the reversible hydrogen electrode (VRHE) can be considered equal to the overall cell voltage. We hereafter refer to the samples before and after the accelerated stress test as the fresh and spent catalysts, respectively.
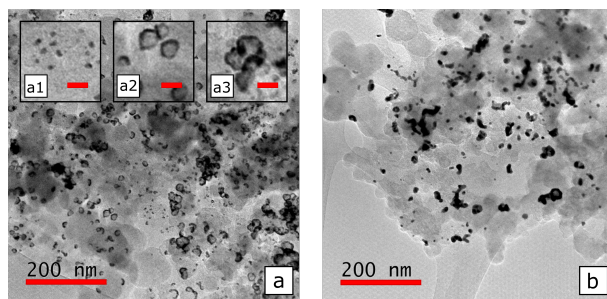
Fig. 1. Transmission Electron Micrographs of the PtNi hollow nanoparticles, in the fresh (a) and spent catalysts (b). The nanoparticles are the smaller black objects and the larger grey objects belong to the carbon support. The insets (a1 to a3) are three magnified views of nanoparticle types coexisting in the fresh catalyst; the scale bars in the insets are 40 nm long.

Figure 1 shows transmission electron microscopy (TEM) images of the catalysts, before and after the stress test. The fresh catalyst contains a large number of relatively well-defined hollow nanoparticles as shown in Fig. 1a2. The material is, however, very heterogeneous as the latter well-defined nanostructures coexist with much smaller compact objects (Fig. 1a1) as well as with larger and very distorted hollow structures (Fig. 1a3). The nanoparticles in the spent catalyst (Fig. 1b) are also extremely distorted, but they are mostly dense and slightly larger.

In addition to TEM, the collapse of the nanostructures during the stress test is confirmed electrochemically by CO stripping, which technique provides an independent measurement of the surface area of the metal nanoparticles (Chattot *et al.*, 2020). The so-obtained area, combined with the known metal loading of 20.4 wt. %, yields a specific surface area $a = 45 \pm 7$ m^2/g$_{Pt}$ in the fresh catalyst. The metal surface area per unit of mass of the entire material (carbon and metal) decreases by 54 % during the stress test. In the meantime the specific metal loading, estimated through STEM/X-EDS, increases to about 30 wt. % as a consequence of support oxidation. The specific surface area of the metal particles is therefore difficult to estimate accurately in the spent catalyst. As an order of magnitude, however, half of the particles

surface is lost during the stress test.

The small-angle x-ray scattering (SAXS) signals from the various sample powders –
contained in either Kapton capillary (fresh catalyst) or Kapton tape (spent catalyst) –
illuminated with a 70 keV X-ray beam were collected at beamline ID31 at ESRF with
a Dectris Pilatus CdTe 2M detector positioned 6.5 m behind the sample. The signal
was protected from air-scattering by a flight tube under mild vacuum. The energy,
detector distance and tilts were calibrated using a standard Ag behenate powder and
the 2D scattering patterns were reduced to 1D curves using pyFAI software package
(Ashiotis *et al.*, 2015). The scattering by the empty carbon support was measured on
a slightly different setup (Gommes *et al.*, 2019). In all cases, the scattering data were
corrected for the contribution of the empty sample holder. The SAXS patterns of the
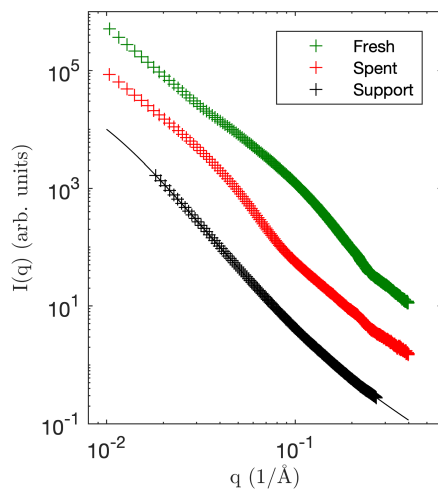porous support as well as of the fresh and spent catalysts are shown in Figure 2.

Fig. 2. Small-angle x-ray scattering (SAXS) patterns of the fresh and spent catalysts,
as well as of the unloaded porous support. The solid black line is the model used
to extrapolate the support contribution over the same angular range as that of the
catalysts.

3. The particle model

3.1. General procedure

We develop a general model of particles aimed at capturing the various types of disordered structures present in the fresh and spent catalysts (see Fig. 1). The central mathematical concept in the model is that of Gaussian Random Field (GRF) (Quiblier, 1984; Berk, 1987), which assigns to any point of space $\mathbf{x}$ a stochastically-defined value $Y(\mathbf{x})$. An isotropic GRF can be thought of as the following sum (Berk, 1991; Levitz, 1998)

$$Y(\mathbf{x}) = \sqrt{\frac{2}{N}} \sum_{n=1}^{N} \sin\left[\mathbf{q}_n \cdot \mathbf{x} - \varphi_n\right] \qquad (1)$$

where $\mathbf{q}_n$ is a vector with random orientation and modulus $q = |\mathbf{q}|$ drawn from a prescribed isotropic distribution with probability density $f_Y(q)4\pi q^2 \mathrm{d}q$, and φ_n is a random phase uniformly distributed in $[0, 2\pi)$. In Eq. (1), the sum is over N contributions; in the limit of $N \to \infty$ the values of $Y(\mathbf{x})$ are Gaussian-distributed with a mean of zero, and the factor $\sqrt{2/N}$ ensures that the variance is equal to one. The GRF is therefore comprehensively characterized by the function $f_Y(q)$, which we refer to as its power-spectral density.

A characteristic of a GRF that is mathematically equivalent to $f_Y(q)$ is its correlation function defined as $g_Y(r) = \langle Y(\mathbf{x})Y(\mathbf{x} + \mathbf{r})\rangle$ where the brackets stand for the ensemble average, *i.e.* the average evaluated over different realizations. The correlation function is related to the power spectral density $f_Y(q)$ via the following Fourier transform (Berk, 1991)

$$g_Y(r) = \int_0^\infty \frac{\sin[qr]}{qr} f_Y(q)4\pi q^2 \ \mathrm{d}q \qquad (2)$$

For reasons that will be clear shortly, we consider only Gaussian fields with a correlation function that is quadratic for small values of r, which enables us to define the

characteristic length l_Y through the relation

$$g_Y(r) \simeq 1 - (r/l_Y)^2 + \ldots \tag{3}$$

close to $r = 0$. Because the functions $g_Y(r)$ and $f_Y(q)$ are Fourier transforms of each other, the length l_Y can also be obtained from the power-spectral density. The relation is

$$\frac{1}{l_Y^2} = \frac{1}{6} \int_0^\infty q^2 f_Y(q) 4\pi q^2 \mathrm{d}q \tag{4}$$

Qualitatively, the length l_Y can be thought of as the distance over which the values of $Y(\mathbf{x})$ change significantly.

Examples of Gaussian fields are provided in Fig. 3. Those fields are obtained with a correlation function of the type

$$g_Y(r) = 1/\cosh\left[\frac{r}{l_Y}\sqrt{2}\right] \tag{5}$$

with $l_Y = 30$ nm (Fig. 3a) and $l_Y = 10$ nm (fig. 3b). The specific function in Eq. (5) is a particular case of a more general function used in earlier work (Gommes & Roberts, 2008; Gommes & Roberts, 2018); it behaves as an exponential over large distances but it is also quadratic at the origin as imposed by Eq. (3). The corresponding power-spectral density is

$$f_Y(q) = \frac{\pi^3}{q l_Y} l_Y^3 \frac{\sinh[\pi q l_Y/(2\sqrt{2})]}{1 + \cosh[\pi q l_Y/\sqrt{2}]} \tag{6}$$

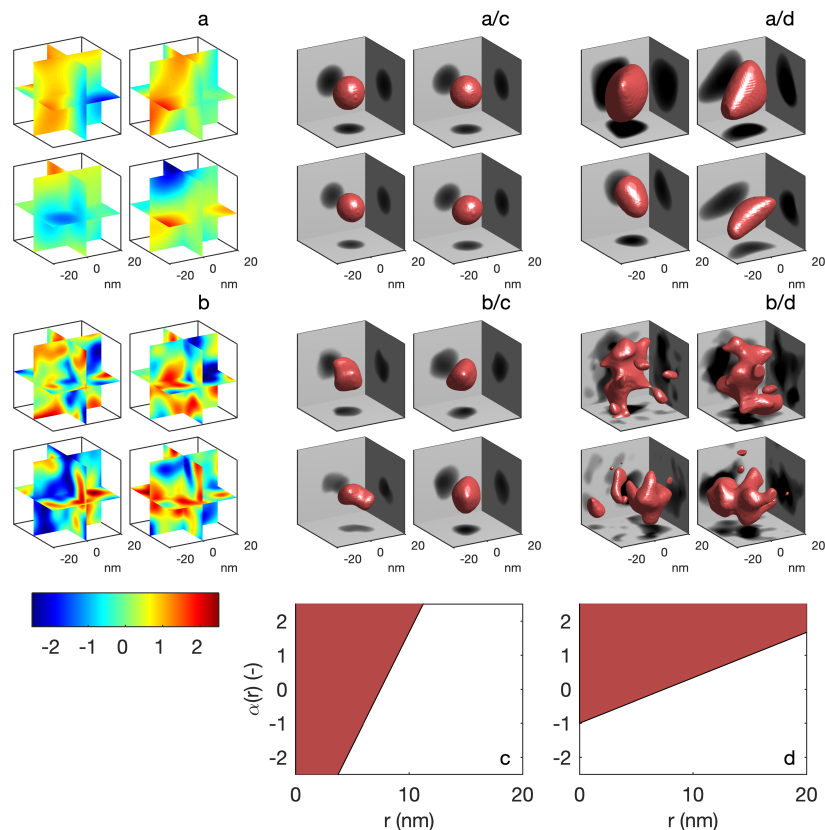as obtained from a Fourier transformation of $g_Y(r)$.

Fig. 3. Modelling of disordered dense nanoparticles, with Gaussian random fields $Y(\mathbf{x})$ having characteristic lengths $l_Y = 15$ nm (a) and 5 nm (b), clipped with two different radial functions $\alpha(r)$ (c and d). The resulting particles are shown in a/c, a/d, b/c and b/d; in each case four realisations are shown to highlight the variability of the particles within one given model. The coloured areas in c and d highlight the region corresponding to the solid.

A classical procedure for modelling disordered co-continuous structures – such as porous materials, emulsions, phase-separated copolymers, etc. – consists in clipping a Gaussian field (Quiblier, 1984; Berk, 1987; Teubner, 1991). With those models, a given phase of a material is modelled as the points of space where a GRF takes values larger than a user-defined threshold. The particle models we discuss here are based on a generalization of this procedure, by which the classical constant threshold is replaced by a space-dependent function $\alpha(\mathbf{x})$ (Gommes & Pirard, 2009). In mathematical terms, the indicator function of the particles $\mathcal{I}(\mathbf{x})$ – taking the value 1 if point $\mathbf{x}$ is in the

particle and 0 otherwise – is defined as

$$\mathcal{I}(\mathbf{x}) = H\left[Y(\mathbf{x}) - \alpha(\mathbf{x})\right] \tag{7}$$

where $H[x]$ is Heaviside's step function (equal to one for $x > 0$ and to zero otherwise), $Y(\mathbf{x})$ is a Gaussian random field, and $\alpha(\mathbf{x})$ is any user-specified space-dependent function.

The procedure is illustrated in Fig. 3 with a Gaussian field having a power spectral density of the type of Eq. (6), and a linear clipping functions of the type

$$\alpha(r) = \alpha_0 + r/l_\alpha \tag{8}$$

where r is the distance from the origin, and l_α and α_0 are two parameters of the model. As shown in Fig. 3, a variety of morphologies can be modelled with this procedure, depending on the values of the parameters.

In the limit of infinitely large values of l_α, the clipping function reduces to a constant α_0 and one recovers the classical clipped Gaussian field model (Levitz, 1998; Gommes, 2018). It is also interesting to note that the opposite limit, *i.e.* small values of l_α correspond to a polydisperse sphere model (see Fig. 3a/c). Spherical particles are indeed obtained whenever the Gaussian field $Y(\mathbf{x})$ is almost constant over distances typical of $\alpha(r)$, which corresponds to the asymptotic limit $l_Y/l_\alpha \gg 1$. In that limit, the points of space where $Y(\mathbf{x}) > \alpha(\mathbf{x})$ make up a sphere with radius

$$r = l_\alpha(Y - \alpha_0) \tag{9}$$

where Y is the local value of the field, which is spatially constant in the limit $l_Y \gg l_\alpha$. Because Y is Gaussian-distributed with a mean of zero and a variance of one, the particle model reduces to spheres with Gaussian-distributed radii with average $\langle r \rangle = -l_\alpha \alpha_0$ and variance $\sigma_R^2 = \langle (r - \langle r \rangle)^2 \rangle = l_\alpha^2$.

When the field $Y(\mathbf{x})$ is variable over distances comparable with l_α the model yields morphologies more complex than spheres. The variety of morphologies include

smoothly deformed particles (Fig. 3a/d), and particles with local bulges protruding out of the surface (Fig. 3b/c). Extremely complex, and occasionally disconnected structures, are obtained for shallow clipping functions, that is for $\alpha_0 \simeq 0$ and $l_\alpha > l_Y$ (Fig. 3b/d).

It is useful to stress here that the small-angle scattering patterns of polydispersed spherical particles and of distorted particles with a gaussian surface are expected to be distinctly different. Indeed, the two types of structures might lead to similar average density profiles but the surface area of distorted particles is necessarily larger. As a consequence the low-q part of the scattering patterns might be similar in both cases, but the Porod scattering in the high q regions will be different.
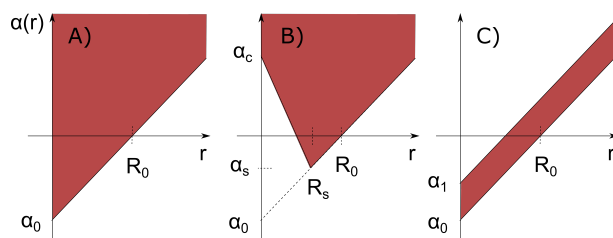
3.2. Hollow particles

Fig. 4. Sketch of the three clipping functions $\alpha(r)$ used to model dense (model A) and hollow (models B and C) particles. The coloured areas highlight the region corresponding to the solid.

The model described in Fig. 3 can only produce dense particles because the clipping function takes its smallest value $\alpha = \alpha_0$ at $r = 0$ (see Fig. 4A). From now on we refer to that first model as model A, and we introduce two generalisations towards hollow structures. The first generalisation is sketched in Fig. 4B. Using a clipping function with large values for $r = 0$ makes the particle hollow. The corresponding clipping function has two additional parameters α_c and α_s, in addition to l_α and α_0. Formally,

the clipping function of our model B is defined as

$$\alpha(r) = \begin{cases} \alpha_c + (r/R_s)(\alpha_s - \alpha_c) & \text{for} \quad r \leq R_s \\ \alpha_0 + r/l_\alpha & \text{for} \quad r > R_s \end{cases} \tag{10}$$

where $R_s = l_\alpha(\alpha_s - \alpha_0)$ can be thought of as the radial position of the shell, *i.e.* where $\alpha(r)$ takes its lowest value α_s. On the other hand, the parameter α_c controls the probability for the center of the particle to be dense or hollow. Realizations of model B are shown in Fig. 5b, in which the hollow centres are indeed visible.
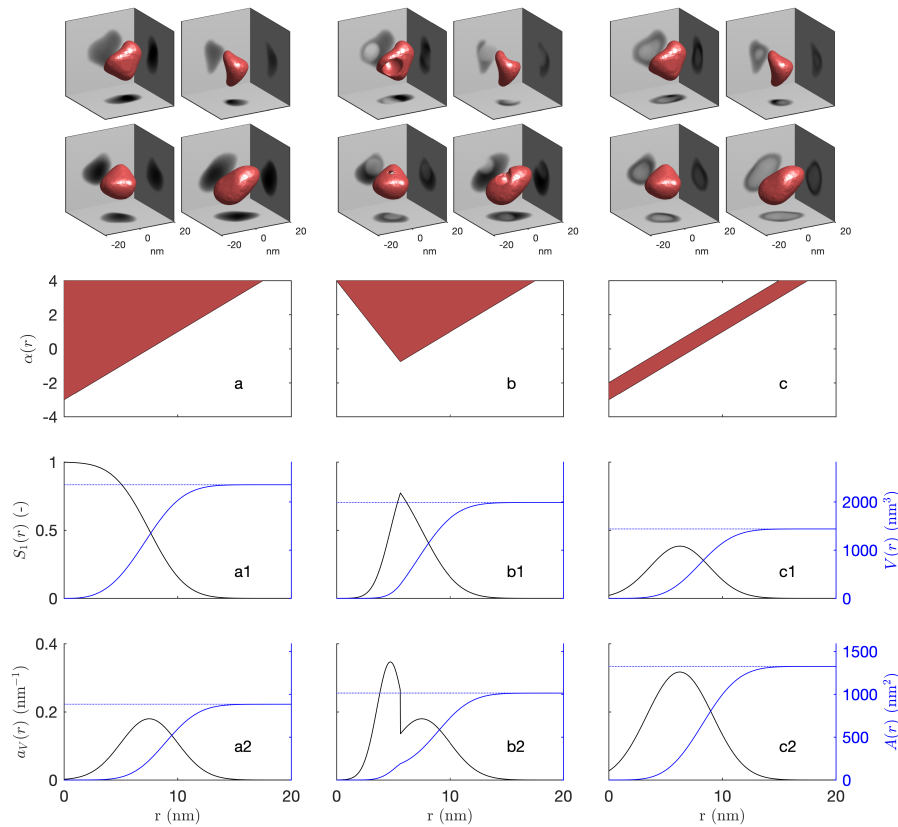

Fig. 5. Realizations of the particle models A, B and C corresponding to the clipping functions (in a, b and c), obtained with a Gaussian field having characteristic length $l_Y = 10$ nm. The density profiles $S_1(r)$ are shown in a_1, b_1 and c_1, and the specific surface profiles $a_V(r)$ are in a_2, b_2 and c_2. The right axes display the cumulated volumes and areas $V(r)$ and $A(r)$ as a function of distance from the center (in blue), with horizontal lines calculated from Eq. (14) for the volumes, and Eq. (19) for the areas.

In some circumstances it might be desirable to have a model that ensures that the inner cavity of the particle is closed. This can be achieved by modifying the clipping procedure as sketched in Fig. 4C. In that case, two clipping functions are used and the particle is modelled as the points of space where the Gaussian field is intermediate between the two functions, say $\alpha(r)$ and $\beta(r)$. In the simple case shown Fig. 4C, the two functions are linear with the same slope, which can be written as

$$\alpha(r) = \alpha_0 + r/l_\alpha$$
$$\beta(r) = \alpha_1 + r/l_\alpha \tag{11}$$

so that the model has a total of three parameters: α_0 and l_α control the size and shape of the outer surface of the particle, and $\alpha_1 - \alpha_0$ controls the thickness of the shell. Realizations of this model are shown in Fig. 5c. The indicator function of model C is formally defined as

$$
\begin{aligned}
\mathcal{I}(\mathbf{x}) &= H[Y(\mathbf{x}) - \alpha(\mathbf{x})]\left(1 - H[Y(\mathbf{x}) - \beta(\mathbf{x})]\right) \\
&= H[Y(\mathbf{x}) - \alpha(\mathbf{x})] - H[Y(\mathbf{x}) - \beta(\mathbf{x})]
\end{aligned} \tag{12}
$$

where the second equality results from assuming $\alpha(\mathbf{x}) \leq \beta(\mathbf{x})$ everywhere, which is the case for Eq. (11). To understand why this procedure leads to hollow particles with a continuous shell, one can notice that the clipping functions $\alpha(r)$ and $\beta(r)$ define the outer and inner surfaces of the particles. The condition $\beta(r) > \alpha(r)$ therefore ensures that the inner and outer surfaces do never touch each other, so that there is no hole in the shell.

3.3. Particles average volume and area

The volume and surface area of the particles defined in figures 3 and 5 are random variables, because they depend on the particular realization of the Gaussian field $Y(\mathbf{x})$. This does not preclude one from calculating average values for the particles volume

and area. For example, the volume of a particle is defined as the integral over the entire space of the indicator function, namely

$$V = \int dV_x \, \mathcal{I}(\mathbf{x}) \tag{13}$$

Because the ensemble averaging commutes with the space integration, the average volume is obtained as

$$\langle V \rangle = \int dV_x \, S_1(\mathbf{x}) \tag{14}$$

where we have used the classical notation $S_1(\mathbf{x}) = \langle \mathcal{I}(\mathbf{x}) \rangle$ for the one-point probability function (Torquato, 2002). The latter function is the probability for a given point of space to be in the solid phase of the particle.

In the case of models A and B, with indicator function defined in Eq. (7), the one-point probability function $S_1(\mathbf{x})$ is calculated as the probability for a Gaussian variable to take values larger than the threshold function $\alpha(\mathbf{x})$ at that specific position. Because the threshold is a radial function, this can be written as

$$S_1(r) = \Lambda_1[\alpha(r)] \tag{15}$$

where we used the notation (Roberts & Knackstedt, 1996)

$$\Lambda_1[\alpha] = \langle H[Y - \alpha] \rangle \tag{16}$$

where Y is a Gaussian variable and $H[x]$ is Heaviside's step function. In terms of the error function erf$[x]$, the function Λ_1 can be calculated as

$$\Lambda_1[\alpha] = \frac{1}{2} - \frac{1}{2}\mathrm{erf}\left[\frac{\alpha}{\sqrt{2}}\right] \tag{17}$$

In the case of model C, the one-point probability function is calculated as

$$S_1(r) = \Lambda_1[\alpha(r)] - \Lambda_1[\beta(r)] \tag{18}$$

which results from Eq. (12) with $\beta(r) \geq \alpha(r)$. Equation 18 is the probability for a Gaussian variable to be larger than $\alpha(r)$ and smaller than $\beta(r)$.

The one-point probability function $S_1(r)$ is equal to the average density at distance r from the origin, calculated over independent realizations of the particles. Examples of average density profiles of models A, B and C are shown in Fig. 5a$_1$ to 5c$_1$. In the case of model A, the average density has a maximum in the centre. By contrast the average density of hollow-particle models B and C has a maximum at some intermediate distance r, corresponding to the most-probable position of the shell. The particles volumes are then obtained through Eq. (14), which in spherical coordinates writes $\int S_1(r) 4\pi r^2 \, \mathrm{d}r$. The cumulative volumes $V(r)$, defined as the average particle volume at distance lower than r to the centre, are plotted in Figs. 5a$_1$, b$_1$ and c$_1$. The horizontal asymptotes in the same graphs are the average volumes of the entire particles.

The surface area of a particle is also a random variable. Its average value is calculated as

$$\langle A \rangle = \int \mathrm{d}V_x \; a_V(\mathbf{x}) \tag{19}$$

where $a_V(\mathbf{x})$ is the average surface area in an infinitesimal volume centred on point $\mathbf{x}$. A general expression for a_V was derived by Gommes & Pirard (2009), namely

$$a_V(\mathbf{x}) = \frac{2^{3/2}}{\pi l_Y} \exp[-\alpha^2/2] \times \Sigma \left[\frac{l_Y |\nabla \alpha|}{2} \right] \tag{20}$$

where α and $\nabla \alpha$ are the local values of the clipping function and of its gradient, and $\Sigma[x]$ is the following function

$$\Sigma[x] = \frac{1}{2} \exp[-x^2] + \left(x + \frac{1}{2x} \right) \frac{\sqrt{\pi}}{2} \mathrm{erf}[x] \tag{21}$$

In Eq. (20), the first factor is the classical expression $a_V = 2^{3/2}/(\pi l_Y) \exp[-\alpha^2/2]$ valid for the classical clipped GRF model (Berk, 1991; Teubner, 1991), and the factor Σ accounts for the gradient of the clipping function. The surface area profiles of models A, B calculated from Eq. (20) are plotted in Fig. 5a$_2$ and 5b$_2$. In the case of model A, the value of $a_V(r)$ is maximum at some intermediate distance r corresponding to the average position of the particle surface. For model B, a more complex pattern

is observed resulting from the existence of an inner and outer surfaces. In the case of model C, there are two contributions to the local surface area density a_V. The contribution of the outer surface is calculated through Eq. (20) and that of the inner surface is calculated through Eq. (20) with α replaced by β. In Fig. 5c$_2$, the two contributions cannot be discriminated because of the small thickness of the shell.

The average total surface area of a particle $\langle A \rangle$ is calculated numerically from Eqs. (19), *i.e.* as $\int a_V(r) 4\pi r^2 \mathrm{d}r$ in spherical coordinates, with $a_V(r)$ calculated from Eq. (20) for arbitrary clipping function $\alpha(r)$ and $\beta(r)$. The corresponding cumulated areas $A(r)$, corresponding to the average surface area at distance smaller than r to the centre, are plotted in in Figs. 5a$_2$, b$_2$ and c$_2$. The horizontal lines are the asymptotes, equal to the total surface area of the particles.

3.4. Particles form factor

The form factor $P(\mathbf{q})$ is the intensity scattered by a single particle (Sivia, 2011). In a stochastic context this is conveniently calculated in two steps, by evaluating first the scattering amplitude $\mathcal{A}(\mathbf{q})$ and then the average value of the squared modulus $|\mathcal{A}(\mathbf{q})|^2$. In terms of the particle indicator function $\mathcal{I}(\mathbf{x})$, the amplitude is

$$\mathcal{A}(\mathbf{q}) = \int \mathrm{d}V_x \; e^{-i\mathbf{q}\cdot\mathbf{x}} \mathcal{I}(\mathbf{x}) \tag{22}$$

which is a random variable because it depends on the values of the indicator function. From Eq. (22), the scattered intensity is then calculated as

$$P(\mathbf{q}) = \int \mathrm{d}V_1 \int \mathrm{d}V_2 \; e^{-i\mathbf{q}\cdot(\mathbf{x}_1-\mathbf{x}_2)} S_2(\mathbf{x}_1, \mathbf{x}_2) \tag{23}$$

which results from expressing $P(\mathbf{q}) = \langle \mathcal{A}(\mathbf{q})\mathcal{A}^*(\mathbf{q}) \rangle$, where the star stands for complex-conjugation. In Eq. (23), the function $S_2(\mathbf{x}_1, \mathbf{x}_2)$ is the two-point probability function defined as

$$S_2(\mathbf{x}_1, \mathbf{x}_2) = \langle \mathcal{I}(\mathbf{x}_1) \mathcal{I}(\mathbf{x}_2) \rangle \tag{24}$$

This ensemble average can be interpreted as the probability that the two points $\mathbf{x}_1$ and $\mathbf{x}_2$ both belong to the solid phase of the particle (Torquato, 2002).

In the present context of clipped Gaussian-field models, with indicator function defined in Eq. (7), the two-point probability function is conveniently expressed in terms of the following error function

$$\Lambda_2[\alpha_1, \alpha_2, g_{12}] = \langle H[Y_1 - \alpha_1]H[Y_2 - \alpha_2]\rangle \tag{25}$$

which generalises the function $\Lambda_1[\alpha]$ introduced in Eq. (16) to the case of two Gaussian variables. Equation (25) is the probability for two Gaussian variables Y_1 and Y_2 with correlation g_{12} to simultaneously be larger than α_1 and α_2, respectively. In principle this can be calculated as the two-dimensional integral of a bivariate Gaussian distribution, but it is easier to evaluate it numerically via the following one-dimensional integral (Berk, 1991; Roberts & Teubner, 1995)

$$\Lambda_2[\alpha_1, \alpha_2, g_{12}] = \Lambda_1[\alpha_1]\Lambda_1[\alpha_2] + \frac{1}{2\pi} \int_0^{\mathrm{asin}[g_{12}]} \exp\left[-\frac{\alpha_1^2 + \alpha_2^2 - 2\alpha_1\alpha_2 \sin(x)}{2\cos^2(x)}\right] \, \mathrm{d}x \tag{26}$$

With this notation, the two-point probability function of models A and B is expressed as

$$S_2(\mathbf{x}_1, \mathbf{x}_2) = \Lambda_2[\alpha(\mathbf{x}_1), \alpha(\mathbf{x}_2), g_Y(\mathbf{r})] \tag{27}$$

where $\mathbf{r} = \mathbf{x}_1 - \mathbf{x}_2$ is the distance between the two points, and $g_Y(\mathbf{r})$ is the correlation between the values of the Gaussian field at those two points, defined in Eq. (2).

It is customary in the scattering literature to define the correlation function $C(\mathbf{r})$ as the intersection volume of a particle and a copy of it that has been translated by a distance $\mathbf{r}$ (Guinier & Fournet, 1955; Glatter & Kratky, 1982; Sivia, 2011). In a stochastic context such an intersection volume is a random variable, the average value of which is obtained as the integral of $S_2(\mathbf{x}_1, \mathbf{x}_2)$ over all pairs of points at vectorial

distance $\mathbf{r}$ from one another, namely

$$C(\mathbf{r}) = \int S_2\left(\mathbf{x} + \frac{1}{2}\mathbf{r}, \mathbf{x} - \frac{1}{2}\mathbf{r}\right) dV_x \tag{28}$$

With this definition of $C(\mathbf{r})$, the double integral in Eq. (23) reduces to the Fourier transform of the correlation function $C(\mathbf{r})$, and one recovers the classical expression for the form factor.

In the case of models A and B the clipping functions are radial, which simplifies the evaluation of $C(r)$. In particular, from Eq. (27), the two-point probability $S_2(\mathbf{x}_1, \mathbf{x}_2)$ does not depends on six variables (two points, each in three-dimensional space) but only on three variables, namely: the radial positions of the two points $r_1 = |\mathbf{x}_1|$ and $r_2 = |\mathbf{x}_2|$ (because the clipping function α is radial) as well as on the distance $r = |\mathbf{x}_1 - \mathbf{x}_2|$ between them (through the field correlation $g_Y(r)$, which is also a radial function). We write this dependence as $S_2\{r_1, r_2, r\}$, with curled brackets. The integral in Eq. (28) is then conveniently calculated in spherical coordinates, in which the radial distance to the origin is ρ, and the polar angle θ is measured with respect to the direction of $\mathbf{r}$. With these coordinates, the radial positions of the two points $\mathbf{x} + \mathbf{r}/2$ and $\mathbf{x} - \mathbf{r}/2$ are

$$r_1 = \sqrt{\rho^2 + (r/2)^2 + \rho r \cos(\theta)} \tag{29}$$

$$r_2 = \sqrt{\rho^2 + (r/2)^2 - \rho r \cos(\theta)} \tag{30}$$

The correlation function is then obtained as

$$C(r) = 4\pi \int_0^\infty \rho^2 d\rho \int_0^1 d\mu \ S_2\left\{\sqrt{\rho^2 + (r/2)^2 + \rho r \mu}, \sqrt{\rho^2 + (r/2)^2 - \rho r \mu}, r\right\} \tag{31}$$

which results from the integral in Eq. (28) through a change of variable $\mu = \cos[\theta]$. The form factor is then obtained as a Fourier transform, *i.e.*

$$P(q) = \int_0^\infty \frac{\sin[qr]}{qr} C(r) 4\pi r^2 \mathrm{d}r \tag{32}$$

which holds for any statistically isotropic particles. The correlation functions and form factors of model A are illustrated in Fig. 6 with a few examples. Although the model is formally identical to the one shown in Fig. 3, different values of the parameters α_0, l_α and l_Y were used here to demonstrate the versatility of the model.
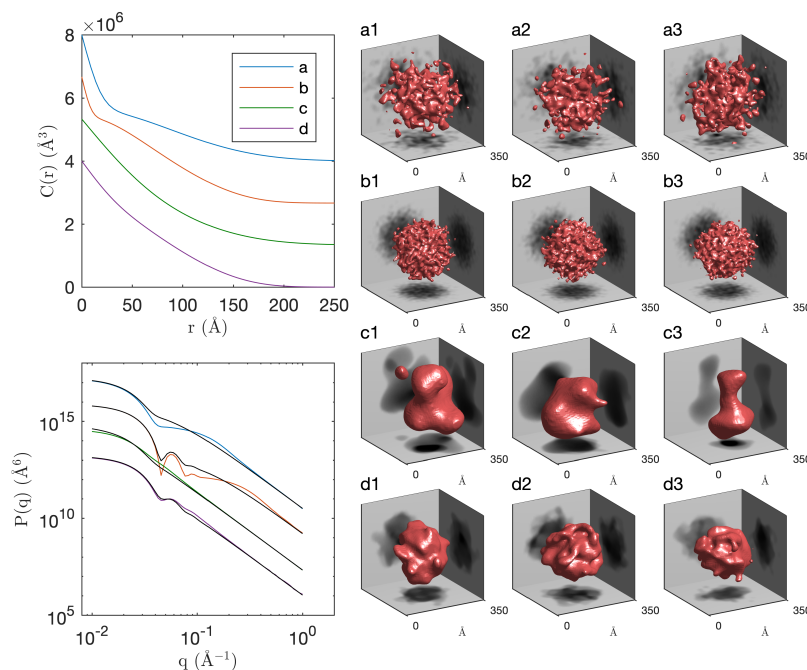

Fig. 6. Correlation functions and form factors for dense particles (model A) with: (a) $\alpha_0 = -2$, $l_Y = l_\alpha/2$; (b) $\alpha_0 = -5$, $l_Y = l_\alpha/2$; (c) $\alpha_0 = -2$, $l_Y = 2l_\alpha$; (d) $\alpha_0 = -5$, $l_Y = 2l_\alpha$, and the value of l_α chosen to have a volume of 8000 nm^3. The coloured lines are the exact results and the black lines are the approximate form factors calculated through Eq. (40). For each set of parameters, three independent realizations are shown.

The mathematical expressions obtained here are valid for any radial clipping function $\alpha(r)$, which includes model B of hollow particles as in Eq. (10). However, in the case of model C with two clipping functions $\alpha(r)$ and $\beta(r)$ a different procedure is needed. The two-point probability function of model C is calculated as

$$S_2(\mathbf{x_1}, \mathbf{x_2}) = \Lambda_2[\alpha(\mathbf{x_1}), \alpha(\mathbf{x_2}), g_Y(\mathbf{r})] - \Lambda_2[\alpha(\mathbf{x_1}), \beta(\mathbf{x_2}), g_Y(\mathbf{r})]$$

$$- \quad \Lambda_2[\beta(\mathbf{x}_1), \alpha(\mathbf{x}_2), g_Y(\mathbf{r})] + \Lambda_2[\beta(\mathbf{x}_1), \beta(\mathbf{x}_2), g_Y(\mathbf{r})] \qquad (33)$$

This equation results from Eq. (24) with the indicator function of model C taken from Eq. (12). The correlation function $C(r)$ is then evaluated via Eq. (28), which leads to four contributions similar to Eq. (31). Examples of hollow particles with their correlation functions are shown in Fig. 7.
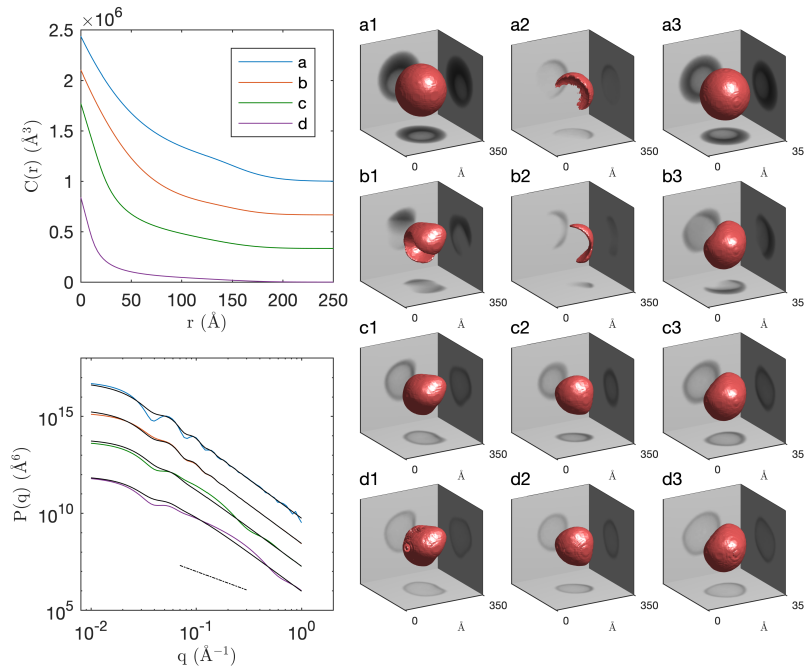

Fig. 7. Correlation functions and form factors for hollow particles obtained through model B with $\alpha_c = 4$, $\alpha_s = 0$ and $l_Y = 30$ nm (a) and $l_Y = 10$ nm (b), as well as through model C with $l_Y = 20$ nm and $\alpha_1 = -2$ (c) and $\alpha_1 = -2.5$ (d). In all cases $\alpha_0 = -3$ and $l_\alpha = 3.75$ nm. The coloured lines are the exact results and the black lines are the approximate form factors calculated through Eq. (40). The dashed line is a $1/q^2$ trend, distinctive of scattering by thin films. For each set of parameters, three independent realisations are shown.

The form factors of both dense and hollow particles (Figs. 6 and 7) exhibit a flat plateau at small q and a Porod-like q^{-4} scattering at high q. The shape of the particles is manisfest in the intermediate q range, with occasional oscillations in $P(q)$ in case of

more ordered structures, as in Fig. 6b. An interesting characteristic of model C (Fig. 7c and 7d) is the presence of an intermediate range of q with a scattering proportional to q^{-2}. This power law is typical of scattering by thin films (Ciccariello *et al.*, 2016), and it accounts for the shell of the hollow particle. When the shell becomes thinner the high-q limit of the q^{-2} extends to higher values of q, as is visible when comparing Figs. 7c and 7d.

4. Discussion

4.1. Approximate expression for the form factor

The exact expression of the form factor $P(q)$ derived in Sec 3.4 can be cumbersome to use in practice because it involves a sequence of numerical integrations. First the two-point probability function $S_2(\mathbf{x}_1, \mathbf{x}_2)$ is calculated as a one-dimensional integral through Eq. (26). Then that function is integrated over a two-dimensional domain through Eq. (31). Finally the result has then to undergo a Fourier transformation to evaluate $P(q)$. Here, we introduce a general approximation for the form factor of any particle in terms of the radial density and specific area profiles $S_1(r)$ and $a_V(r)$ (see Fig. 5). In addition to its practical usefulness (*e.g.* in the context of a data fitting procedure), the approximate expression developed here helps us validate the exact analytical results of Sec. 3.4.

Our approximation is based on the following two mathematical constraints that any two-point correlation function $S_2(\mathbf{x}_1, \mathbf{x}_2)$ must satisfy (Ciccariello & Benedetti, 1985; Torquato, 2002). First, in the case where the two points are far away from each other, the values of the indicator function at $\mathbf{x}_1$ and $\mathbf{x}_2$ are statistically independent from each other, which leads to

$$S_2(\mathbf{x}_1, \mathbf{x}_2) \simeq S_1(\mathbf{x}_1)S_1(\mathbf{x}_2) \tag{34}$$

Second, when $\mathbf{x}_1$ and $\mathbf{x}_2$ are close to each other, the correlation decreases propor-

tionally to the distance $\mathbf{x}_1 - \mathbf{x}_2$ and to the local value of the specific surface area. Specifically, using the notation $\mathbf{x}_2 = \mathbf{x}_1 + r\hat{\omega}$ where $\hat{\omega}$ is a unit vector, the following relation holds

$$\frac{1}{4\pi} \int d\hat{\omega} \; S_2(\mathbf{x}_1, \mathbf{x}_1 + r\hat{\omega}) \simeq S_1(\mathbf{x}_1) - \frac{a_V(\mathbf{x}_1)}{4} r \qquad (35)$$

for small values of r (Gommes & Pirard, 2009). In this equation, the left-hand side is the average value of $S_2(\mathbf{x}_1, \mathbf{x}_2)$ over all points $\mathbf{x}_2$ at a distance r from $\mathbf{x}_1$, and $a_V(\mathbf{x}_1)$ is the specific surface area at point $\mathbf{x}_1$. In the particular case of clipped Gaussian fields the local surface area can be calculated through Eq. (20), but Eq. (35) applies to any two-phase structure.

The two constraints in Eqs. (34) and (35) are valid for large and small distances r, respectively. The approximation we introduce consists in assuming that the transition between the two regimes is exponential and isotropic, namely

$$S_2(\mathbf{x}_1, \mathbf{x}_2) \simeq S_1(\mathbf{x}_1) S_1(\mathbf{x}_2) + S_1(\mathbf{x}_1) \left[1 - S_1(\mathbf{x}_1)\right] \exp \left[\frac{-|\mathbf{x}_1 - \mathbf{x}_2|}{l(\mathbf{x}_1)} \right] \qquad (36)$$

This general functional form ensures that $S_2(\mathbf{x}_2, \mathbf{x}_2) = S_1(\mathbf{x}_2)$ and that $S_2(\mathbf{x}_1, \mathbf{x}_2) = S_1(\mathbf{x}_1) S_1(\mathbf{x}_2)$ for $|\mathbf{x}_1 - \mathbf{x}_2| \gg l(\mathbf{x}_1)$. Moreover, if the local characteristic length that enters the exponential is chosen to be

$$l(\mathbf{x}) = 4 \frac{S_1(\mathbf{x})[1 - S_1(\mathbf{x})]}{a_V(\mathbf{x})} \qquad (37)$$

one can check that Eq. (35) is satisfied for small values of r.

Evaluating the Fourier transform of Eq. (36) via Eq. (23) provides the following approximation for the form factor

$$P(\mathbf{q}) = P_1(\mathbf{q}) + 8\pi \int dV_x \; \frac{S_1(\mathbf{x})[1 - S_1(\mathbf{x})]l^3(\mathbf{x})}{[1 + [ql(\mathbf{x})]^2]^2} \qquad (38)$$

The first contribution is the Fourier transform of the particle average density, namely

$$P_1(\mathbf{q}) = \left| \int dV_x \; e^{-i\mathbf{q}\cdot\mathbf{x}} S_1(\mathbf{x}) \right|^2 \qquad (39)$$

which is a low-q approximation. The second contribution is a high-q correction that accounts for the possible presence of many solid/void interfaces at a scale much smaller than that of the particle as a whole. As a consequence of the exponential approximation introduced in Eq. (36), this is calculated here as a sum of Debye-Bueche contributions of all the infinitesimal volumes that make up the particle (Gommes, 2018).

In the particular case of statistically isotropic particles, which is notably the case for all models considered in Sec. 3, the approximate form factor simplifies to

$$P(q) = P_1(q) + 8\pi \int_0^\infty 4\pi r^2 \mathrm{d}r \; \frac{S_1(r)[1 - S_1(r)]l^3(r)}{[1 + [ql(r)]^2]^2} \tag{40}$$

with

$$P_1(q) = \left| \int_0^\infty 4\pi r^2 \mathrm{d}r \; \frac{\sin(qr)}{qr} S_1(r) \right|^2 \tag{41}$$

Equation (40) is plotted as solid black lines in Fig. 6 in the case of model A of dense particles, and in Fig. 7 for hollow particles. Globally, the approximate form factor in Eq. (40) captures reasonably well the exact value for small and large values of q. In particular, the asymptotic form of Eq. (40) reduces to Porod's law

$$P(q) = 2\pi \frac{\langle A \rangle}{q^4} \tag{42}$$

for high values of q, where $\langle A \rangle = \int \mathrm{d}V_x \; a_V(\mathbf{x})$ is the average total surface area of the particles. Expectedly, deviations between exact and approximate form factors are observed for intermediate values of q. This is notably the case for model C hollow particles, for which the q^{-2} intermediate scattering is not captured (see Fig. 7d).

It is interesting to note that the contribution $P_1(q)$ to the approximate form factor in Eq. (40) depends only on the average density of the particles $S_1(r)$. That specific contribution to the scattering does therefore not depend on the characteristic length of the Gaussian field l_Y. Accordingly, the contribution $P_1(q)$ alone would not enable one to discriminate, say, the scattering of polydispersed sphere from that of Gaussian particles with distorted surface. However, the second contribution to Eq. (40)

is calculated from the specific surface area profile $a_V(r)$. That term enables one to discriminate geometrical distorsion from mere polydispersity, based on the high-q part of the SAS signal.

4.2. Fitting the SAXS of supported hollow nanoparticles

The Gaussian-field models of particles were used to analyse the SAXS patterns of the fresh and spent catalysts presented in Sec. 2. For that purpose, it is necessary to account first for the relative contribution of the particles and of the porous carbon support to the measured scattered intensity. The total scattering is (Gommes *et al.*, 2019)

$$I(q) = \rho_s^2 I_s(q) + \rho_p^2 \theta_p P(q) \qquad (43)$$

where ρ_s and ρ_p are the electron densities of the material that make up the solid and the particles, respectively; $I_s(q)$ is the scattering contribution of the solid; θ_p is the average number of particles per unit volume of the entire material, and $P(q)$ is their form factor. In general, the scattering by supported nanoparticles contains cross-correlation terms, which are ignored in Eq. (43). This approximation is valid in the case of low loading of the support, *i.e.* if the average electron density of the pore-filling phase (as if the particles were homogeneously dispersed in the pores) is much lower than that of the solid phase of the support (Gommes *et al.*, 2019). As we shall discuss shortly, this applies to the catalysts of Sec. 2.

The scattering by the support is modelled as a Debye-Bueche contribution

$$I_s(q) = \frac{8\pi\phi_s(1-\phi_s)l_D^3}{(1+(ql_D)^2)^2} + \frac{b}{q^2} \qquad (44)$$

where ϕ_s is the volume fraction of the solid, l_D is a characteristic length of the material, and the second contribution proportional to b accounts for the turbostratic structure of carbon (Perret & Ruland, 1968). The solid contribution was fitted to the SAXS data of the empty support as thoroughly explained in Gommes *et al.* (2019); the best

fit is shown in Fig. 2 as a solid black line corresponding to parameters $\phi_s = 0.17$, $l_D = 158$ Å and $b = 1.85$ Å. Although there is evidence that the support partially oxydises during the stress test, we assume here that its structure remains unchanged so that we can use the support contribution to the SAXS is the same in the fresh and spent catalysts.

The other material constants that enter Eq. (43) are the electron densities of the support and of the particles, ρ_s and ρ_p, and the particle concentration θ_p. The electron densities are assumed to be $\rho_s = 0.9$ Faraday/cm^3 for the carbon support and $\rho_p = 8.6$ Faraday/cm^3 for the particles, assuming they are made up of pure Pt with traces of Ni (Gommes et $al.$, 2019). The particle concentration θ_p is calculated from the known metal loading and the average particle volume $\langle V \rangle$. Assuming that the carbon making up the support has specific mass of 2 g/cm^3 and that the particles consist mostly of Pt with specific mass of 21.5 g/cm^3, the overall loading of 20.4 wt. % Pt/C converts to a volume fraction $\phi_p \simeq 0.004$, which means that the metal occupies about 0.4 % of the entire volume of the material. Using that value, the particle concentration is then calculated as a function of the average particle volume as

$$\theta_p = \frac{\phi_p}{\langle V \rangle} \tag{45}$$

Incidentally, from the volume fraction of metal ϕ_p one calculates that the average electron density of the pore-filling phase is 0.04 Faraday/cm^3, which is much smaller than the electron density of carbon, and justifies ignoring cross-correlation effects in Eq. (43).
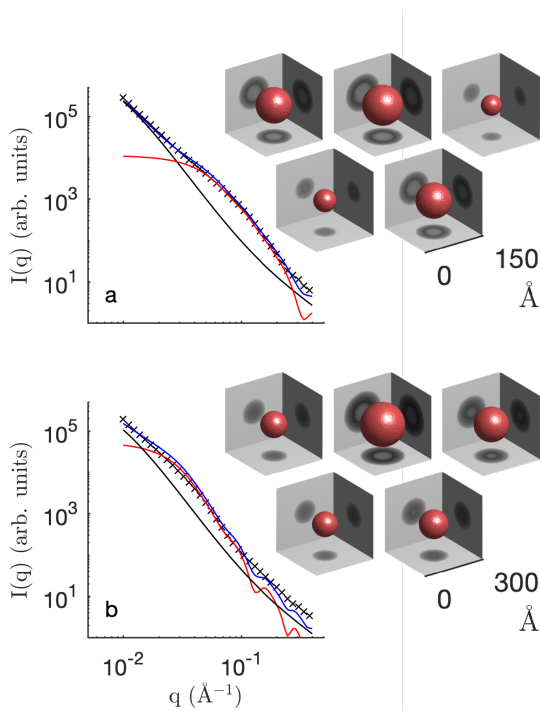
Fig. 8. Fitting of the SAXS of the fresh (a) and spent (b) catalysts (see Figs. 1 and 2) with a polydispersed hollow sphere model. The crosses are the data and the blue line is the best fit, with the contributions of the solid support in black and of the particles in red. In each case five realisations of the particle model are shown, together with their projections.

As a benchmark for our analysis, we first fit the SAXS of the catalysts with a classical spherical-shell model (Pedersen, 1997). For the fitting, the inner radii R_i of the particles are assumed to be distributed according to a gamma distribution, having average inner radius $\langle R_i \rangle$ and shape parameter k. For large values of k the gamma distribution is narrowly peaked around the average value, and the distribution broadens with decreasing k. The lowest admissible value is $k = 1$, for which the gamma distribution reduces to an exponential. Moreover, all particles are assumed to have the same shell thickness t independently of their inner radius. The fitting of the SAXS data with three adjustable parameters – $\langle R_i \rangle$, k and t – is shown in Fig. 8. For both the fresh and spent catalysts, the procedure converges to the lowest admissible value for the

shape parameter of the distribution, $k = 1$, which points to extremely polydispersed structures. The values of the other fitted parameters are gathered in Tab. 1.

Assuming that the particles are made of pure Pt, the geometrical surface areas can be calculated from the model parameters (Gommes, 2018), yielding the values $a = 51$ m^2/g$_{Pt}$ and $a = 21$ m^2/g$_{Pt}$ in the fresh and spent catalysts. These values compare well with those obtained from CO stripping reported in Sec. 2, namely 45 $\pm$ 7 m^2/g$_{Pt}$ in the fresh catalyst and a value approximately two times smaller in the spent catalyst. In addition, we also use the fitted parameter to calculate the following two global shape descriptors. The average chord length of the particles l_C is calculated as $l_C = 4\langle V \rangle / \langle A \rangle$, where $\langle V \rangle$ and $\langle A \rangle$ are the average particle volume and areas. The sphericity ψ is calculated as $\psi = \pi^{1/3}(6\langle V \rangle)^{2/3}/\langle A \rangle$, and it takes values between 0 and 1. The value $\psi = 1$ corresponds to a sphere, and values smaller than 1 point to particles with a surface area much larger than the sphere with the same volume. The average chord length l_C and the sphericity ψ are distinct and complementary characteristics of the particles. The average chord length characterises the size of solid parts of the particle. The sphericity is a dimensionless quantity that is independent of the particle size: it is a measure of how compact an object is, independently of its size. The values of ψ reported in Tab. 1 for the spherical-shell model are relatively close to 1. This is a consequence of the shell thickness t being larger than the average inner radius $\langle R_i \rangle$. Globally, the fitting of the SAXS with the spherical-shell model suggests that the particles becomes larger and more compact during the accelerated stress test.

Table 1. *Values of the model parameters (spherical shell as well as stochastic models B and C) obtained from the least-square fits of the SAXS data on the fresh and spent catalysts. For each model the specific surface area a, the average chord length l_C, and the sphericity ψ is calculated from the fitted parameters. The statistical uncertainty on all fitted parameters is lower than 1 %.*

			Fresh Catalyst	Spent Catalyst
Spherical shell	$\langle R_i \rangle$	(Å)	10	15
	k	(-)	1^a	1^a
	t	(Å)	21	54
	a	(m^2/g$_{Pt}$)	51	21
	l_C	(Å)	3.6	8.9
	ψ	(-)	0.85	0.93
Model B	l_Y	(Å)	40	95
	l_α	(Å)	91	164
	α_0	(-)	0	-0.2
	R_s	(Å)	85	89
	a	(m^2/g$_{Pt}$)	53	20
	l_C	(Å)	3.5	9.1
	ψ	(-)	0.32	0.39
Model C	l_Y	(Å)	139	96
	l_α	(Å)	128	167
	α_0	(-)	-1.18	-0.15
	α_1	(-)	-0.87	2
	a	(m^2/g$_{Pt}$)	54	21
	l_C	(Å)	3.5	9.1
	ψ	(-)	0.16	0.4

[a] lowest value allowed

Although the spherical-shell model fits fairly the SAXS data, it forces the reality into a type of structure that is not representative of all particles in the samples. The spherical shell could at best describe the type of particles shown in inset a2 of Fig. 1, which are not the only type of structures present in the fresh catalyst. Moreover, these hollow structures seem to be altogether absent in the spent catalyst (Fig. 1b). We therefore also fitted the SAXS data with the stochastic models presented in Sec. 3.2. Model B is in general described by 5 parameters: the characteristic length of the Gaussian field l_Y, the two parameters l_α and α_0 that describe the outer surface of the particle (similar to those of model A), and the two parameters α_s and α_c that describe the inner hollow core. In order to reduce the number of fitting parameters to 4, we impose that the absolute value of the slope of $\alpha(r)$ is the same on both sides of R_s (see

Fig. 4). This is equivalent to assuming that the inner and outer limits of the shell are of comparable sharpness. Mathematically, we use the the radial position of the shell R_s as a fitting parameter, from which one evaluates $\alpha_s = \alpha_0 + R_s/l_\alpha$ and $\alpha_c = \alpha_s + R_s/l_\alpha$. The best fits are illustrated in Fig. 9, and the corresponding parameters are in Tab. 1. The SAXS data were also fitted with model C of hollow particle, and the best fits are shown in Fig. 10. Model C has a total of four parameter: the characteristic length l_Y of the Gaussian field, the characteristic length of the clipping function l_α, and the two values α_0 and α_1. The best fits are illustrated in Fig. 10, and the corresponding parameters are in Tab. 1.
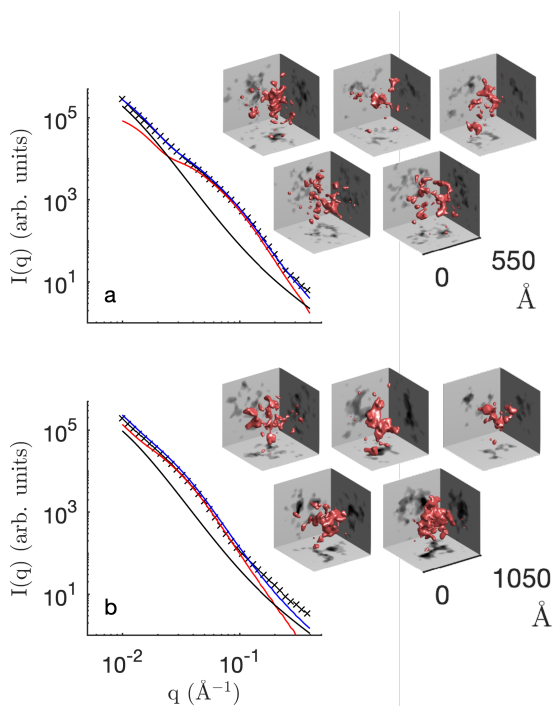

Fig. 9. Fitting of the SAXS of the fresh (a) and spent (b) catalysts (see Figs. 1 and 2) with stochastic model B (see Fig. 5). The crosses are the data and the blue line is the best fit, with the contributions of the solid support in black and of the particles in red. In each case five realisations of the particle model are shown, together with their projections.
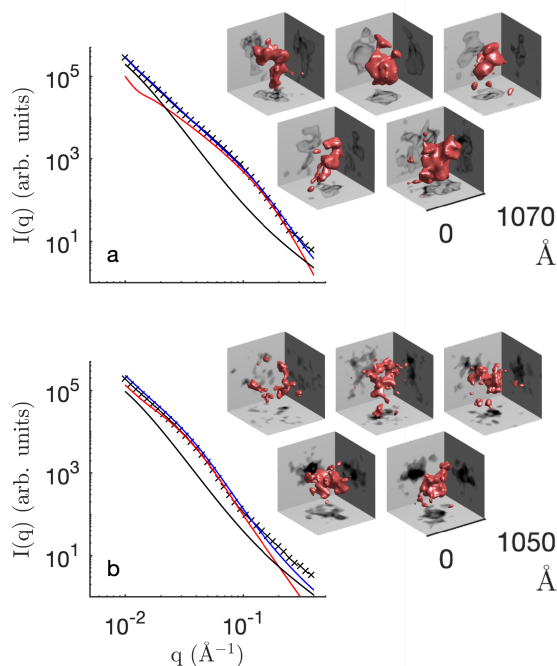
Fig. 10. Fitting of the SAXS of the fresh (a) and spent (b) catalysts (see Figs. 1 and 2) with stochastic model C (see Fig. 5). The crosses are the data and the blue line is the best fit, with the contributions of the solid support in black and of the particles in red. In each case five realisations of the particle model are shown, together with their projections.

When comparing the outcome of the SAXS fitting with models B and C, it is interesting to note that the two models yield very similar particle morphologies for the spent catalysts (see Figs 9b and 10b). The realisations and their projections shown in the figure are also qualitatively similar to those visible in TEM micrographs (Fig 1b). Mathematically, the two models are strictly equivalent in the limit of very small values of R_s (model B) or large values of α_1 (model C), in which case they reduce to model A of dense nanoparticles. The values of the fitted parameters in Tab. 1 show that this is approximately the case for the spent catalyst. The average density profiles in Fig. 11 hint at slightly hollow particles for model B and dense particles for model C. These differences appear to be very minor based on the values of the sphericity,

which hint at relatively dense structures in the spent catalyst for both models B and C.
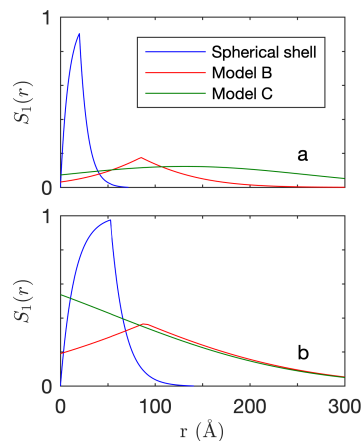

Fig. 11. Average density profiles corresponding to the three models fitted to the SAXS data of the fresh (a) and spent (b) catalysts.

In the case of the fresh catalysts, the morphologies obtained through the fitting of models B and C are distinctly different as visible from the realisations in Figs. 9a and 10a. Model B seems to yield a structure consisting in disordered parts randomly distributed in space. On a closer examination, however, the density profile (Fig. 11a) is seen to exhibit a clear maximum with $S_1 \simeq 0.2$ at a distance of approximately 80 Å from the centre. The structure can therefore be thought of as a hollow nanoparticle with approximate diameter of 160 Å and a 80 %-porous shell. With such high porosity the shell is actually made up of disconnected lumps. Such disconnected structure is physically unrealistic. The overall quality of the fit hints at the fact that all connected parts of the shell do not carry sufficient statistical weight to contribute significantly to the scattering pattern. It has also to be kept in mind that the catalyst is extremely heterogeneous as it contains objects with very different sizes (see Fig. 1a1-a3). The fitting procedure accounts in a statistical way for the scattering by all the different

types of structures in the sample.

Contrary to model B, the very construction of model C guarantees the connectivity of the particle shell. The least-square fit copes with this structural constraint by producing objects that are significantly larger than those of model B, but very distorted and with a very thin shell (Fig. 10a). It is the size of the local bulges in these bigger objects that compares with the structures captured by model B. The different types of structures produced by models B and C are further illustrated with the density profiles shown in Fig. 11a.

It is interesting to compare the outputs of the spherical-shell model and of the two stochastic models. Some features, such as the specific surface area a and the average chord length l_C are remarkably consistent throughout all models. (see Tab. 1) This was expected because they can both be expressed in terms of the surface-to-volume ratio of the particles, which can in principle be obtained from a Porod analysis of the scattering patterns without any model. (Ciccariello *et al.*, 1988; Gommes, 2018) Moreover, the values are also consistent with those obtained independently from CO stripping (see Sec. 2).

By contrast, other characteristics are strongly dependent on the model, as is notably the case for the sphericity ψ. These differences point to the qualitatively different types of structures that are implicitly assumed when one chooses a specific model over another one. In particular, based on the values of ψ, the spherical shells are relatively compact objects when compared to stochastic models B and C, and model C is the least compact structure. As a consequence, stochastic models B and C predict objects that are much larger than the spherical-shell model. This is particularly clear when comparing the density profiles in Fig. 11. Moreover the spherical-shell model strongly underestimates the size of the particles, as is apparent when comparing the density profiles with the insets of Fig. 1 One has therefore to conclude that the structures

captured by the spherical-shell model are merely local features of the bigger structures that are better captured by the two stochastic models.

5. Conclusions

We have developed and discussed a family of stochastic models of disordered particles. The models generalise the classical clipped Gaussian-field models of continuous structures by using a space-dependent clipping function instead of a constant. Depending on the clipping procedure a variety of morphologies can be produced. The focus of the present work was on dense and hollow nanostructures, but the same procedure can be used for other types of more complex structures. All the analytical formulae derived here for the volume (Eqs. 14 and 15), area (Eqs. 19 and 20), and correlation function (Eq. 31) are valid for any radial clipping function $\alpha(r)$. The generalisation to anisotropic structures is straightforward, only numerically more cumbersome. This can also be generalised towards polyphasic structures with no more conceptual difficulties than for deterministic models. A possibility consists in modelling the scattering-length density of the material as a piecewise-constant function, with each region of constant density being defined stochastically (Gommes, 2013).

Although the data analysis procedure developed in the paper produces realistic real-space illustrations of the structure, one has to keep in mind that this is achieved through a modelling. Models cannot be avoided in this context because there are generally a large number of structures compatible with any given correlation function (Gommes *et al.*, 2012). The very purpose of models is to bias the reconstruction process so as to reduce its degeneracy. In classical deterministic models, the bias is generally towards geometrical simplicity. With stochastic models, the bias is towards geometrical disorder. Preferring one approach over the other is a matter of modelling choice, which has to be based on the specific type of material being investigated.

In the case of stochastic models, the morphological significance of the parameters is occasionally difficult to visualise. In particular the models capture the variability of the structures from one particle to the next, which is why several independent realisations were systematically shown for any given set of parameters. A convenient way to visualise the *average* geometry of a given particle model is through their density and surface-area profiles, for which we obtained general expressions. We also derived an approximation of the form factor based on the latter two profiles, which coincides with Porod's and Guinier's laws in the limits of high and low values of q, respectively. That approximation (Eq. 40) is particularly useful in the context of data fitting because it can be evaluated much faster than the exact expression, which requires numerically evaluating a two-dimensional integral followed by Fourier transformation. In our fitting procedure, the approximation was used for the coarse and manual screening of the parameters, followed by the proper least-square minimisation with the exact expression.

We used the developed models to analyse the SAXS data of two PtNi hollow nanoparticles samples, before and after being used during oxygen-reduction catalysis, which were both known from microscopy to have very disordered and heterogeneous structures. The data can be reasonably fitted with a classical spherical shell form factor, but this procedure forces the data into a model that is geometrically too simple In consequence, the fitted structure has little qualitative resemblance with the actual sample and the sizes are systematically underestimated. By contrast, the stochastic models yield more realistic geometries.

References

Ashiotis, G., Deschildre, A., Nawaz, Z., Wright, J. P., Karkoulis, D., Picca, F. E. & Kieffer, J. (2015). *J. Appl. Cryst.* **48**, 510–519.

Berk, N. F. (1987). *Phys. Rev. Lett.* **58**(25), 2718–2721.

Berk, N. F. (1991). *Phys. Rev. A*, **44**(8), 5069–5079.

Carl, N., Müller, W., Schweins, R. & Huber, K. (2020). *Langmuir*, **36**(1), 223–231.

Chattot, R., Le Bacq, O., Beermann, V., Khl, S., Herranz, J., Henning, S., Kühn, L., Asset, T., Guétaz, L., Renou, G., Drnec, J., Bordet, P., Pasturel, A., Eychmüller, A., Schmidt, T. J., Strasser, P., Dubau, L. & Maillard, F. (2018). *Nature Mater.* **17**(9), 827–833.

Chattot, R., Martens, I., Scohy, M., Drnec, J., Maillard, F. & Dubau, L. (2020). *ACS Energy Lett.* **5**(1), 162–169.

Chen, S. H., Lee, D. D., Kimishima, K., Jinnai, H. & Hashimoto, T. (1996). *Phys. Rev. E*, **54**(6), 6526–6531.

Ciccariello, S. & Benedetti, A. (1985). *J. Appl. Cryst.* **18**, 219–229.

Ciccariello, S., Goodisman, J. & Brumberger, H. (1988). *J. Appl. Cryst.* **21**, 117–128.

Ciccariello, S., Riello, P. & Benedetti, A. (2016). *J. Appl. Cryst.* **49**, 260–276.

Glatter, O. & Kratky, O. (1982). *Small Angle X-ray Scattering*. New York: Academic Press.

Gommes, C. J. (2013). *J. Appl. Cryst.* **46**(2), 493–504.

Gommes, C. J. (2018). *Microp. Mesop. Mater.* **257**, 62–78.

Gommes, C. J., Asset, T. & Drnec, J. (2019). *J. Appl. Cryst.* **52**, 507–519.

Gommes, C. J., Jiao, Y. & Torquato, S. (2012). *Phys. Rev. E*, **85**(5), 051140.

Gommes, C. J. & Pirard, J. P. (2009). *Phys. Rev. E*, **80**(6), 061401.

Gommes, C. J. & Roberts, A. P. (2008). *Phys. Rev. E*, **77**(4), 041409.

Gommes, C. J. & Roberts, A. P. (2018). *Phys. Chem. Chem. Phys.* **20**, 13646–13659.

Grillo, I. (2009). *Curr. Op. Coll. Interf. Sci.* **14**(6), 402 – 408.

Guinier, A. & Fournet, G. (1955). *Small Angle Scattering of X-rays*. New York: John Wiley.

Levitz, P. (1998). *Adv. Coll. Interf. Sci.* **76-77**, 71–106.

Narayanan, T., Diat, O. & Bösecke, P. (2001). *Nucl. Instr. Meth. Phys. Res. A*, **467-468**(PART II), 1005–1009.

Pedersen, J. S. (1997). *Adv. Coll. Interf. Sci.* **70**, 171–210.

Perret, R. & Ruland, W. (1968). *J. Appl. Cryst.* **1**, 308–313.

Pipich, V., Balz, M., Wolf, S. E., Tremel, W. & Schwahn, D. (2008). *J. Am. Chem. Soc.* **130**(21), 6879–6892.

Quiblier, J. A. (1984). *J. Coll. Interf. Sci.* **98**(1), 84–102.

Roberts, A. & Knackstedt, M. A. (1996). *Phys. Rev. E*, **54**(3), 2313–2328.

Roberts, A. P. & Teubner, M. (1995). *Phys. Rev. E*, **51**, 4141–4154.

Sivia, D. S. (2011). *Elementary Scattering Theory*. Oxford: Oxford University Press.

Stribeck, N. (2010). *X-Ray Scattering of Soft Matter*. Berlin: Springer.

Teubner, M. (1991). *Europhys. Lett.* **14**, 403–408.

Torquato, S. (2002). *Random Heterogeneous Materials*. New York: Springer.

Synopsis

We propose a versatile model of disordered nanoparticles for the purpose of analysing small-angle scattering data. Our approach generalises the classical clipped Gaussian field models of random structures, by allowing the clipping function to be space dependent.